Reactive-infiltration instability in radial geometry: From dissolution fingers to star patterns

Piotr Grodzki and Piotr Szymczak
Institute of Theoretical Physics, Faculty of Physics, University of Warsaw, Pasteura 5, 02-093 Warsaw, Poland

(Received 22 July 2019; published 13 September 2019)

We consider the process of chemical erosion of a porous medium infiltrated by a reactive fluid in a thin-front limit, in which the width of the reactive front is negligible with respect to the diffusive length. We show that in the radial geometry the advancing front becomes unstable only if the flow rate in the system is sufficiently high. The existence of such a stable region in parameter space is in contrast to the Saffman-Taylor instability in radial geometry, where for a given flow rate the front always eventually becomes unstable, after reaching a certain critical radius. We also examine the similarities between the reactive-infiltration instability and the similar instability in the heat transfer, which is driving the formation of star-like patterns on frozen lakes.

DOI: 10.1103/PhysRevE.100.033108

I. INTRODUCTION

A planar dissolution front propagating through a homogeneous porous matrix is unstable with respect to small variations in local permeability; regions of high permeability dissolve faster because of enhanced transport of reactants, which leads to increased rippling of the front. This phenomenon, usually referred to as reactive-infiltration instability [1,2], is an important mechanism for pattern development in geology, with a range of morphologies and scales, from cave systems running for hundreds of miles to laboratory acidization on the scale of centimeters [3–14]. In general, this instability is characterized by two length scales [15]: the diffusive length (D/v) and the reactant penetration length ($v/\kappa s$), where v is the Darcy velocity, D is the diffusion constant, κ is the dissolution rate, and s is the specific reactive area. If the latter scale is much smaller than the former, then one can adopt the so-called thin front limit, where the interface is treated as a discontinuity in porosity, with a completely dissolved phase on one side and an undissolved phase on the other. Linear stability analysis for this case has been carried out by Chadam *et al.* [1], and the corresponding dispersion relation shows that long wavelengths are unstable, whereas short wavelengths are stabilized by diffusion.

In their derivation, Chadam *et al.* have considered rectangular geometry with a pressure gradient applied along the length of the system. However, in many cases (e.g., in the acidization of oil reservoirs) the reactive fluids are injected through a well and thus the relevant geometry is radial rather than rectangular [3,13,16–20]. Motivated by this, here we carry out the linear stability analysis of the reactive-infiltration problem in radial geometry, with the fluid injection at the center of the system. We stay within the thin-front limit and derive the corresponding dispersion relation, $\omega(k)$ which links the growth rate of the instability (ω) with the wave number of the perturbation (k). The dispersion relation shows stable regions for both the long-wavelength and short-wavelength modes, and the unstable region in between. Next, we study how the instability growth rate depends on the Péclet number (Pe) and permeability contrast between the undissolved and dissolved phase (Γ). We find that, in contrast to the rectangular case, there is a region in the (Pe, Γ) space where the system is absolutely stable [$\omega(k) < 0$ for all k]. Next, we draw parallels between the dissolving porous media system and Saffman-Taylor instability [21]. In both cases the more mobile phase invades a less mobile one. In the Saffman-Taylor system, the mobility contrast is due to the lower viscosity of an invading fluid, whereas in reactive-infiltration the higher mobility of the invading (dissolved) phase is due to its increased porosity with respect to the undissolved system. In rectangular geometry, these similarities are manifested in the identical form of $\omega(k)$ relation for small wave vectors (i.e., long waves); however, the short-wave part of the dispersion relation is different, reflecting different short-scale stabilization mechanisms: surface tension in the case of Saffman-Taylor problem versus diffusion for the reactive-infiltration.

In the radial geometry, the differences between the two instabilities become more pronounced. One of them is the existence of a stable region in (Pe, Γ) space for the reactive-infiltration instability. This is in contrast to the Saffman-Taylor instability in radial geometry [22], where for a given flow rate the front always becomes eventually unstable, after reaching a certain critical radius R.

The paper is organized as follows. In Sec. II the general equations governing the dynamics of the dissolving porous rock are introduced. Then, in Secs. III–V we describe approximations introduced in the analysis: the small acid capacity limit and the thin-front limit. Next, in Secs. VI and VII we derive the dispersion relation of the reactive-infiltration instability in radial geometry and analyze the stability of the system in (Pe, Γ) space. The results are discussed in Sec. VIII, where we also examine the similarities between the reactive-infiltration instability and the similar instability in the heat transfer which leads to the formation of star-like patterns on frozen lakes. Finally, the conclusions are drawn in Sec. IX.

II. THE GOVERNING EQUATIONS

When a porous matrix is infiltrated by an incoming flux of reactive fluid, a front develops once all the soluble material

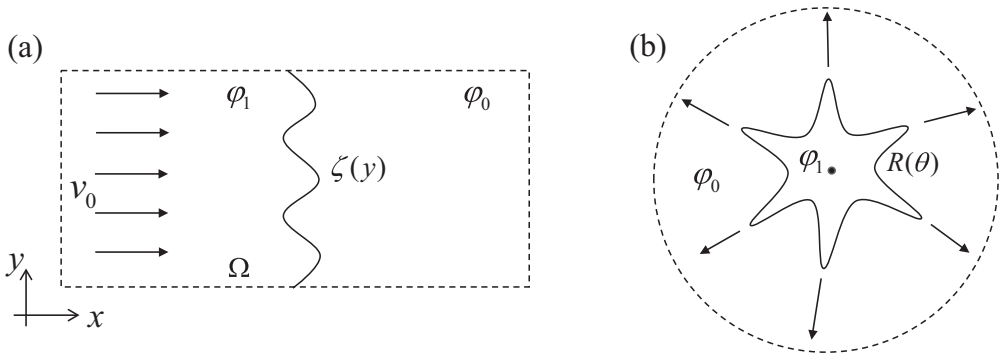

FIG. 1. Geometry of the system. (a) Rectangular geometry: a reactive fluid is injected from the left side and dissolves the porous matrix through chemical reactions. As the dissolution progresses, the reaction front $\zeta(y)$, shown by the solid line, advances into the matrix, separating the fully dissolved, upstream domain (Ω) of porosity φ_1 from the undissolved medium of initial porosity φ_0. (b) Radial geometry: the reactive fluid is injected at the center of the system and dissolves the surrounding matrix. The reaction front, $R(\theta)$ advances outwards.

at the inlet has been dissolved. This front propagates into the matrix as illustrated in Fig. 1, which shows the position of the front (solid line) some time later. Upstream of the front, all the soluble material has dissolved and the porosity is constant, $\varphi = \varphi_1$. Ahead of the front the porosity decays gradually to its value in the undissolved matrix, $\varphi = \varphi_0$.

On scales large compared with the pore size, the velocity of the fluid is proportional to the pressure gradient (Darcy's law),

$$\boldsymbol{v} = -\frac{K(\varphi)}{\mu}\nabla p, \tag{1}$$

where v is the Darcy velocity, φ is the porosity and $K(\varphi)$ is the permeability, which we will assume to be isotropic. When there are chemical reactions leading to the porosity change, the velocity field is no longer divergence free, and the continuity equation is of the form

$$\partial_t \varphi + \nabla \cdot \boldsymbol{v} = 0. \tag{2}$$

The transport of reactants and products is described by a convection-diffusion-reaction equation,

$$\partial_t(\varphi c) + \nabla \cdot (\boldsymbol{v} c) - \nabla \cdot (D\varphi \nabla c) = -\Sigma, \tag{3}$$

where D is the diffusion constant and Σ—the reaction rate.

For simplicity we will assume a linear kinetic equation for the reaction rate,

$$\Sigma(c) = \kappa s c \theta(\varphi_1 - \varphi), \tag{4}$$

where κ is the rate constant and s is the reactive surface area per unit volume. However, our results will turn out to be independent of the exact form of $\Sigma(c)$ assumed. The Heaviside step function in Eq. (4), $\theta(\varphi_1 - \varphi)$, guarantees that the reaction term vanishes in the region where all of the soluble material has dissolved (which corresponds to the porosity $\varphi = \varphi_1$).

Dissolution of the matrix by the reactive fluid gives rise to a time-dependent porosity field,

$$\nu c_{\mathrm{sol}} \partial_t \varphi = \Sigma(c), \tag{5}$$

where c_{sol} is the concentration of the solid species, and ν accounts for the stoichiometry of the reaction.

III. SMALL ACID CAPACITY LIMIT

The acid capacity number $\gamma_a = c_{\mathrm{in}}/\nu c_{\mathrm{sol}}$ is defined as the ratio between volume of rock (of molar concentration c_{sol}) to the volume of reactant (of molar concentration c_{in}) needed to fully dissolve it. In typical geophysical systems the reactant is dilute ($c_{\mathrm{in}} \ll c_{\mathrm{sol}}$) and therefore $\gamma_a \ll 1$; for example, when calcite is dissolved by aqueous CO_2, $\gamma_a \sim 10^{-4}$. Whenever $\gamma_a \ll 1$ the velocity and concentration fields will reach steady state well before any significant change in porosity. This can be formalized by the following change of coordinates and rescaling of the fields:

$$t' = t/t^\star, \quad x' = x/l^\star, \quad y' = y/l^\star \tag{6}$$

$$c' = c/c_{\mathrm{in}}, \quad s' = s/s_0, \quad \boldsymbol{v}' = \boldsymbol{v}/v_0, \quad \varphi' = \varphi/\varphi_0, \tag{7}$$

with

$$t^\star = \frac{1}{\gamma_a \kappa s_0}, \quad l^\star = \frac{D\varphi_0}{v_0}. \tag{8}$$

where s_0 is the specific reactive surface of the undissolved matrix and v_0 is a characteristic flow rate. For example, in rectangular geometry of Fig. 1(a) v_0 corresponds to the velocity of the incoming solution (as $x \to -\infty$).

In these variables the equations take the form:

$$\gamma_a H \frac{\partial \varphi}{\partial t'} + \nabla' \cdot \boldsymbol{v} = 0, \tag{9}$$

$$\gamma_a H \frac{\partial(\varphi c')}{\partial t} + \nabla' \cdot (c' \boldsymbol{v}) = \nabla \cdot (\varphi \nabla c) - H s' c', \tag{10}$$

$$\frac{\partial \varphi'}{\partial t'} = s' c' \theta(\varphi_1' - \varphi'), \tag{11}$$

where

$$H = \frac{D\varphi_0 \kappa s_0}{v_0^2}. \tag{12}$$

In the limit $\gamma_a \to 0$ the flow and transport equations become stationary and read

$$\nabla' \cdot \boldsymbol{v} = 0, \tag{13}$$

$$\nabla' \cdot (c' \boldsymbol{v}) = \nabla \cdot (\varphi \nabla c) - H s' c', \tag{14}$$

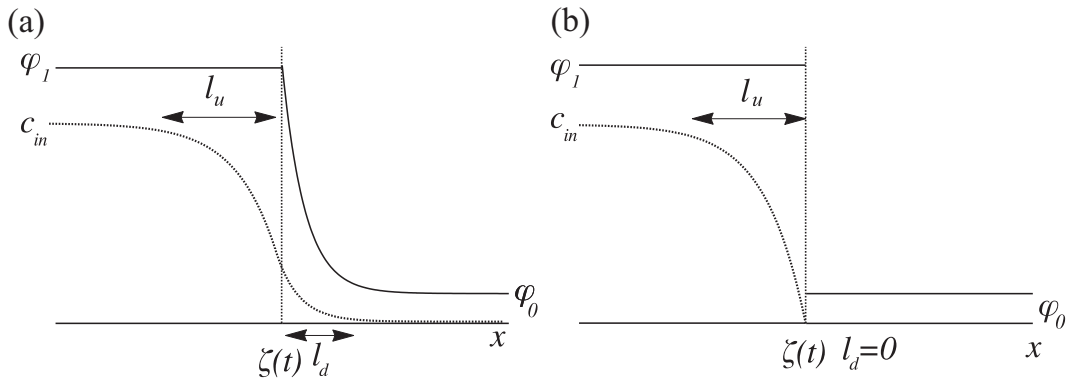

FIG. 2. Concentration and porosity profiles. The concentration profile decays with different length scales, l_u and l_d, in the upstream [$x < \zeta(t)$] and downstream [$x > \zeta(t)$] regions, with $\zeta(t)$ marking the position of a reaction front. Right panel illustrates the thin-front limit, in which $l_u \gg l_d$.

whereas the last equation describes porosity evolution over a longer timescale,

$$\frac{\partial \varphi'}{\partial t'} = s' c' \theta(\varphi_1' - \varphi'). \tag{15}$$

This is the limit that we adopt from now on. Coming back to the original variables we thus have

$$\nabla \cdot \boldsymbol{v} = 0, \tag{16}$$

$$\nabla \cdot (\boldsymbol{v} c) - \nabla \cdot (D\varphi \nabla c) = -\kappa s c \theta(\varphi_1 - \varphi), \tag{17}$$

and

$$\nu c_{\rm sol} \partial_t \varphi = \kappa s c \theta(\varphi_1 - \varphi). \tag{18}$$

IV. UPSTREAM AND DOWNSTREAM PENETRATION LENGTH

Let us for a moment consider a situation, in which the reaction front in Fig. 1 is planar, i.e., the region $x < \zeta(t)$ is completely dissolved ($\varphi = \varphi_1$). In such a case, the flow is uniform, $v = v_0 \hat{\mathbf{e}}_x$ and the transport equation reduces to the 1D form,

$$v_0 \partial_x c - \partial_x (D\varphi \partial_x c) = -\kappa s c \theta(\varphi_1 - \varphi), \tag{19}$$

which has the following solution in the region $x < \zeta$, where the reaction term vanishes (since $\varphi = \varphi_1$ there),

$$c(x) = c_{\rm in}\left(1 - A e^{\frac{x-\zeta}{l_u}}\right), \quad x < \zeta, \tag{20}$$

where $c_{\rm in}$ is the reactant concentration in the inflowing solution and l_u is the upstream penetration length

$$l_u = \frac{D\varphi_1}{v_0}. \tag{21}$$

The solution downstream is more complicated, since porosity is in general a function of x there, but for large x, where $\varphi(x) \to \varphi_0$ we get asymptotically

$$c(x) = B e^{-x/l_d}, \quad x \to \infty, \tag{22}$$

with the downstream penetration length of the form

$$l_d = \frac{D\varphi_0}{v_0} \frac{2}{\sqrt{1+4H}-1}, \tag{23}$$

as illustrated in Fig. 2. The upstream penetration length is of a diffusive character, whereas the downstream length is determined by the interplay of transport and reaction.

V. THIN FRONT LIMIT

The ratio of the downstream and upstream penetration lengths,

$$l_d/l_u = \frac{\varphi_0}{\varphi_1} \frac{2}{\sqrt{1+4H}-1}, \tag{24}$$

is determined by the parameter H. In particular,

$$l_d/l_u \to 0 \quad \text{as} \quad H \to \infty \tag{25}$$

defines so called thin-front limit, with the downstream reactive length negligible in comparison to the upstream diffusive length [1,2,15,23]. In that limit one can assume that the reaction takes place instantaneously with the reactants fully consumed at the dissolution front, as shown in the right panel of Fig. 2. A more detailed discussion of the small acid capacity limit, thin front limit, and their applicability to the physical problems can be found in Ref. [24].

As a consequence, we obtain a Stefan-like problem in which the space is divided into two domains: the dissolved, upstream domain (Ω) of porosity φ_1 and the undissolved, downstream domain ($\bar{\Omega}$) of porosity φ_0, complementary to Ω (cf. Fig. 1).

Geometry of the system is then fully described by the curve $\zeta(y)$ corresponding to the reaction front, which advances with velocity proportional to the flux of the reactant at a given point

$$U_n = -\frac{\gamma_a}{c_{\rm in}(\varphi_1 - \varphi_0)} D\varphi_1 (\nabla c)_n, \quad \mathbf{r} \in \partial\Omega(t), \tag{26}$$

where subscript n represents the component normal to the interface. Only the diffusive flux is present in Eq. (26), since the concentration at the front vanishes, and so does the convective contribution to the flux. Since the porosities in each phase are constant, the pressure obeys Laplace equation in both domains

$$\nabla^2 p_u = 0, \quad \nabla^2 p_d = 0, \tag{27}$$

whereas the concentration field is governed by the convection-diffusion equation

$$\nabla \cdot (\mathbf{v} c_u) - D\varphi_1 \nabla^2 c_u = 0, \tag{28}$$

in the upstream region. In the downstream region, $c_d = 0$. Additionally, both the pressure and the normal component of the Darcy velocity need to be continuous across the reaction front $\partial\Omega$:

$$p_u|_{\zeta(y)} = p_d|_{\zeta(y)}, \tag{29}$$

$$v_{un}|_{\zeta(y)} = v_{dn}|_{\zeta(y)}. \tag{30}$$

VI. RADIAL GEOMETRY

Let us now consider dissolution in the radial geometry. A schematic of the system is presented in Fig. 1(b)—the fluid is injected at the origin of coordinates with a constant rate Q (in m^2/s). In cylindrical coordinate system, the front becomes a function $R(\theta, t)$. The boundary conditions are given by

$$\lim_{r\to\infty} r\boldsymbol{v_d} = \frac{Q}{2\pi}\hat{\mathbf{e}}_r, \tag{31}$$

$$c(r=0) = c_{\text{in}}, \tag{32}$$

$$c[R(\theta)] = 0, \tag{33}$$

$$p_u|_{R(\theta)} = p_d|_{R(\theta)}, \tag{34}$$

$$v_{un}|_{R(\theta)} = v_{dn}|_{R(\theta)}. \tag{35}$$

Let us first consider a uniform case where the solution depends on r only. The reactive front is then a circle of radius $R^0(t)$, increasing in time. The radially symmetric solutions of Eqs. (27) and (28) are then

$$p_u^0 = -\frac{\mu Q}{2\pi K_u}\log\frac{r}{R^0(t)}, \quad p_d^0 = -\frac{\mu Q}{2\pi K_d}\log\frac{r}{R^0(t)}, \tag{36}$$

$$\boldsymbol{v_u}^0 = \boldsymbol{v_d}^0 = \frac{Q}{2\pi r}\hat{\mathbf{e}}_r, \tag{37}$$

where K_u and K_d are the permeabilities of the upstream (downstream) domain and the pressure gauge is chosen such as to guarantee that p vanishes at the reaction front.

Convection-diffusion equation for radially symmetric case reduces to

$$D\varphi_1\frac{1}{r}\frac{\partial}{\partial r}\left(r\frac{\partial c^0}{\partial r}\right) = \frac{Q}{2\pi r}\frac{\partial c^0}{\partial r}, \tag{38}$$

with the solution of the form

$$c^0 = c_{\text{in}}\left[1 - \left(\frac{r}{R^0(t)}\right)^{\text{Pe}}\right] \quad r < R^0, \tag{39}$$

where

$$\text{Pe} = \frac{Q}{2\pi D\varphi_1} \tag{40}$$

is the Péclet number measuring the ratio of convective and diffusive effects in the system. Equation (26) gives then the front velocity of the form

$$\boldsymbol{U}_0 = \frac{\gamma_a}{\varphi_1 - \varphi_0}\frac{Q}{2\pi R^0}\hat{\mathbf{e}}_r. \tag{41}$$

Since $U_0 = \frac{dR^0}{dt}$ we can solve for $R^0(t)$, getting

$$R^0(t) = \sqrt{R_0^2 + \frac{\gamma_a}{\varphi_1 - \varphi_0}\frac{Q}{\pi}t}, \tag{42}$$

where $R_0 = R^0(t=0)$.

VII. LINEAR STABILITY ANALYSIS FOR THE RADIAL CASE

Let us now introduce infinitesimal perturbations of the front position as well as of the pressure, velocity, and concentration fields:

$$R \to R^0(t) + \delta R, \tag{43}$$

$$p_u \to p_u^0 + \delta p_u, \tag{44}$$

$$\boldsymbol{v_u} \to \boldsymbol{v_u^0} + \boldsymbol{\delta v_u}, \tag{45}$$

$$\boldsymbol{c_u} \to \boldsymbol{c_u^0} + \boldsymbol{\delta c_u}, \tag{46}$$

and analogously for the downstream part. The form of the perturbation can be arbitrary, but due to the linearity of the equations allows us to consider individual Fourier components, e.g.,

$$\delta R = \varepsilon F(t)\sin(n\theta), \tag{47}$$

where θ is the polar angle [Fig. 1(b)] and $n \in \mathbf{N}$ is the wave number of the perturbation. Note that, since the base state [Eq. (42)] is time-dependent, the function $F(t)$ will not, in general, be the exponential function of time, as it is the case for the time-independent base states.

The pressure perturbation obeys the Laplace equation

$$\frac{1}{r}\frac{\partial}{\partial r}\left(r\frac{\partial\delta p_i}{\partial r}\right) + \frac{1}{r^2}\frac{\partial^2\delta p_i}{\partial\theta^2} = 0, \tag{48}$$

where $i = d, u$. The velocity perturbation can then be calculated as

$$\boldsymbol{\delta v_i} = -\frac{K}{\mu}\boldsymbol{\nabla}\delta p_i, \tag{49}$$

with the boundary conditions

$$\delta p_u(r=0) = 0, \quad \lim_{r\to\infty} r\boldsymbol{\delta v_d} = 0,$$

$$\left(p_d^0 - p_u^0\right)_{R^0} + (\delta p_d - \delta p_u)_{R^0} + \delta R\left(\frac{\partial p_d^0}{\partial x} - \frac{\partial p_u^0}{\partial x}\right)_{R^0} = 0,$$

$$\delta v_{dr}\Big|_{R^0} + \delta R\frac{\partial v_{dr}^0}{\partial r}\Big|_{R^0} = \delta v_{ur}\Big|_{R^0} + \delta R\frac{\partial v_{ur}^0}{\partial r}\Big|_{R^0}.$$

The first two relations come from the fact that both the pressure at the center and the overall flow rate is fixed. The last two are obtained by linearizing the continuity condition, Eq. (29) at the perturbed front. The solution to the above is

$$\delta p_u = -\varepsilon F(t)\frac{\mu Q}{2\pi R^0}\frac{(R^0)^{-n}}{K_u}\frac{1-\Gamma}{1+\Gamma}r^n\sin(n\theta), \tag{50}$$

$$\delta p_d = \varepsilon F(t)\frac{\mu Q}{2\pi R^0}\frac{(R^0)^{n}}{K_d}\frac{1-\Gamma}{1+\Gamma}r^{-n}\sin(n\theta), \tag{51}$$

where $\Gamma = K_d/K_u$ is the permeability ratio between the downstream and upstream part. The Darcy law can now be used to

calculate $\mathbf{v}_u$:

$$\delta\mathbf{v}_u = \varepsilon F(t)\frac{Q}{2\pi R^0}(R^0)^{-n}n\frac{1-\Gamma}{1+\Gamma}r^{n-1}\sin(n\theta)\hat{\mathbf{e}}_\mathbf{r}. \tag{52}$$

Next we solve for the concentration perturbation. The linearized convection-diffusion equation can be put in the form

$$\frac{1}{r}\frac{\partial}{\partial r}\left(r\frac{\partial\delta c}{\partial r}\right)+\frac{1}{r^2}\frac{\partial^2\delta c}{\partial\theta^2} = \frac{\mathrm{Pe}}{r}\frac{\partial\delta c}{\partial r}+\varepsilon F(t)c_{\mathrm{in}}n\mathrm{Pe}^2\frac{1-\Gamma}{1+\Gamma}\frac{r^{\mathrm{Pe}+n-2}}{(R^0)^{\mathrm{Pe}+n+1}}\sin(n\theta), \tag{53}$$

with Pe given by Eq. (40). The solution of this equation vanishing at $r=0$ is

$$\delta c = \varepsilon\left[Cr^\lambda-\frac{\mathrm{Pe}\varepsilon c_{\mathrm{in}}}{R^0}\frac{1-\Gamma}{1+\Gamma}\left(\frac{r}{R^0}\right)^{\mathrm{Pe}+n}\right]\sin(n\theta)F(t), \tag{54}$$

where

$$\lambda=\frac{\mathrm{Pe}}{2}\left(1+\sqrt{1+4\left(\frac{n}{\mathrm{Pe}}\right)^2}\right). \tag{55}$$

The constant in Eq. (54) can be obtained from the requirement that the perturbation of concentration vanishes at the front

$$c^0(R^0)+\delta R\left.\frac{\partial c^0}{\partial r}\right|_{R^0}+\delta c|_{R^0}=0, \tag{56}$$

which leads to $C=\frac{2}{1+\Gamma}c_{\mathrm{in}}\mathrm{Pe}(R^0)^{-\lambda-1}$, thus finally

$$\delta c=\frac{\mathrm{Pe}\varepsilon F(t)c_{\mathrm{in}}}{R^0(1+\Gamma)}\left[2\left(\frac{r}{R^0}\right)^\lambda-(1-\Gamma)\left(\frac{r}{R^0}\right)^{\mathrm{Pe}+n}\right]\sin(n\theta). \tag{57}$$

Finally, the growth rate of the perturbations can be obtained from δc using Eq. (26) for the front velocity, which, after linearization, yields

$$\frac{\partial\delta R}{\partial t}=-\frac{D\varphi_1\gamma_a}{c_{\mathrm{in}}(\varphi_1-\varphi_0)}\left(\delta R\left.\frac{\partial^2c^0}{\partial r^2}\right|_{R^0}+\left.\frac{\partial\delta c}{\partial r}\right|_{R^0}\right), \tag{58}$$

which leads to the generalized growth rate [22,25] of the form

$$\omega(n)=\frac{\dot F(t)}{F(t)}=\frac{\xi(n)}{[R^0(t)]^2}, \tag{59}$$

with

$$\xi(n)=\frac{D\varphi_1\gamma_a\mathrm{Pe}^2}{(\varphi_1-\varphi_0)(1+\Gamma)}\left[1-\sqrt{1+4\left(\frac{n}{\mathrm{Pe}}\right)^2}+\left(\frac{n}{\mathrm{Pe}}\right)(1-\Gamma)-\frac{1}{\mathrm{Pe}}(1+\Gamma)\right]. \tag{60}$$

As shown in Eq. (42) the dependence of $(R^0)^2$ on t is linear, $[R^0(t)]^2=R_0^2+\beta t$, with $\beta=\frac{\gamma_a}{\varphi_1-\varphi_0}\frac{Q}{\pi}$. For a such a simple form of $R^0(t)$, Eq. (59) can be integrated to yield

$$F(t)=\left(1+\frac{\beta t}{R_0^2}\right)^{\frac{\xi(n)}{\beta}}. \tag{61}$$

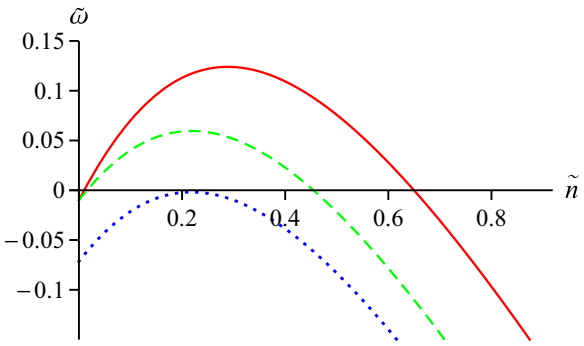

FIG. 3. Dispersion relation in radial geometry for Pe = 100, $\Gamma=0$ (solid line); Pe = 100, $\Gamma=0.2$ (dashed); Pe = 14, $\Gamma=0.2$ (dotted).

This shows that even though the time-dependence of the modes is not a simple exponential, still the fastest growing modes are those with the largest $\omega(n)$ [or $\xi(n)$].

VIII. DISCUSSION

Using Eq. (41) we can rewrite Eq. (59) in the form

$$\omega(n)=\frac{U_0}{l_u(1+\Gamma)}\left[1-\sqrt{1+4\left(\frac{n}{\mathrm{Pe}}\right)^2}+\left(\frac{n}{\mathrm{Pe}}\right)(1-\Gamma)-\frac{1}{\mathrm{Pe}}(1+\Gamma)\right]. \tag{62}$$

As expected, the natural lengthscale for this problem is the upstream penetration length,

$$l_u=\frac{D\varphi_1}{v_0}=\frac{D\varphi_1}{\frac{Q}{2\pi R^0}}, \tag{63}$$

whereas the natural timescale is

$$\tau=l_u/U_0, \tag{64}$$

i.e., the time over which the dissolution front moves over the length l_u. Next, the natural scaling for the wave number is

$$\tilde n=n/\mathrm{Pe}. \tag{65}$$

With these scalings,

$$\tilde\omega(\tilde n)\equiv\tau\omega=\frac{1}{1+\Gamma}[1-\sqrt{1+4\tilde n^2}+\tilde n(1-\Gamma)]-\frac{1}{\mathrm{Pe}}. \tag{66}$$

The dispersion relations corresponding to different values of Pe and Γ are shown in Fig. 3. The region $\tilde n>0$ can be divided in three subintervals: $(0;\tilde n_1)$ which is characterized by stable growth; $(\tilde n_1;\tilde n_2)$, unstable; and $\tilde n>\tilde n_2$, stable again. The threshold values $\tilde n_{1,2}$ are given by

$$\tilde n_{1,2}=\frac{[(1+\Gamma)/\mathrm{Pe}-1](1-\Gamma)}{4-(1-\Gamma)^2}\times\left(1\mp\sqrt{1-\frac{[(1-\Gamma)^2-4]\{[(1+\Gamma)/\mathrm{Pe}-1]^2-1\}}{[(1+\Gamma)/\mathrm{Pe}-1]^2(1-\Gamma)^2}}\right).$$

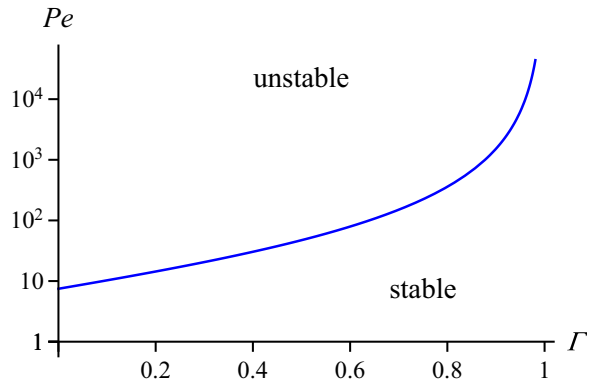

FIG. 4. The threshold Péclet number $\mathrm{Pe}_{\mathrm{thr}}$ as a function of the permeability ratio, Γ.

On the other hand, the most unstable mode is given by

$$\tilde{n}_c = \frac{1-\Gamma}{2\sqrt{4-(1-\Gamma)^2}}, \tag{67}$$

which determines the wavelength of the most unstable mode,

$$\lambda_c = \frac{2\pi R^0}{\tilde{n}_c \mathrm{Pe}} = \frac{4\pi R^0 \sqrt{4-(1-\Gamma)^2}}{(1-\Gamma)\mathrm{Pe}}. \tag{68}$$

As we see, the most unstable wavelength decreases as the flow velocities (and hence Pe) increase. Importantly, λ_c will increase in time as the radial extent of the front R^0 grows. The dispersion relation depends on two parameters only—Pe and Γ. Let us now find the region in Pe–Γ space in which all perturbations are stable, i.e., $\tilde{\omega}(\tilde{n}_c) \leqslant 0$. For given Γ the stable region corresponds to $\mathrm{Pe} < \mathrm{Pe}_{\mathrm{thr}}$ with

$$\mathrm{Pe}_{\mathrm{thr}}(\Gamma) = \frac{2(1+\Gamma)}{2-\sqrt{4-(1-\Gamma)^2}}, \tag{69}$$

as shown in Fig. 4. Importantly, Pe (for a given volumetric flow Q) does not depend on the radial extent of the front, R^0. Consequently, we can find the range of Q such that the front will remain stable during its entire evolution.

A. Relation to the rectangular case

The linear stability analysis of the dissolution front in the rectangular geometry has been carried out in Refs. [1,2,24]. In this case the perturbations of the front are of the form

$$\delta\zeta = \varepsilon e^{\omega t} \sin(ky), \tag{70}$$

where y is the coordinate perpendicular to the flow (cf. Fig. 1). Dispersion relation in this case reads

$$\tilde{\omega}(\tilde{k}) = \frac{1}{1+\Gamma}[(1-\Gamma)\tilde{k} + 1 - \sqrt{1+4\tilde{k}^2}], \tag{71}$$

with $\tilde{k} = k l_u$, where, as before, $l_u = \frac{D\varphi_1}{v_0}$ is the upstream diffusive length. The corresponding timescale, $\tau = l_u/U_0$, has been used here to rescale time.

The largest unstable wave vector (corresponding to the shortest unstable wavelength) is given by

$$\tilde{k}_0 = \frac{2(1-\Gamma)}{4-(1-\Gamma)^2}. \tag{72}$$

The maximum of the dispersion relation corresponds to

$$\tilde{k}_c = \frac{1-\Gamma}{2\sqrt{4-(1-\Gamma)^2}}, \tag{73}$$

which determines the wavelength $\lambda_c = 2\pi D\varphi_1/\tilde{k}_c v_0$ of the most unstable mode. Note that Eq. (73) is fully analogous to Eq. (67) in the radial case.

We note that the dispersion relation for the rectangular geometry, Eq. (71), can be obtained from its radial counterpart, Eq. (66), in the limit, $R^0 \to \infty$, $v_0 = Q/2\pi R^0 = \mathrm{const.}$ (which implies $Q \to \infty$). In this limit $\tilde{n} \to \tilde{k}$, and $\mathrm{Pe} \to \infty$, and we recover Eq. (71).

In fact, this limiting procedure leads to the elimination of the last term $(1/\mathrm{Pe})$ in the right-hand side of Eq. (66), which shifts the entire dispersion curve downwards and results in the appearance of the stable region in the phase diagram of Fig. 4.

Next, let us comment on the differences between the radial and rectangular case. At first sight, it would seem that the key difference between these two cases is the presence of stable region in the Pe–Γ space in the radial growth. However, we need to keep in mind that Eq. (71) was derived for a system of an infinite lateral extent. If, instead, we consider a system of a finite width, W, then only the perturbations with $\lambda < W$ are permissible in the linear stability analysis (assuming periodic boundary conditions along y). For small enough W all admissible perturbations fall into the stable region of the dispersion relation, with $\omega(k) < 0$. Taking into account Eq. (72), the rectangular system will remain stable if

$$\frac{v_0 W}{2\pi D\varphi_1} < \frac{2\pi[4-(1-\Gamma)^2]}{2(1-\Gamma)}. \tag{74}$$

Noting that $v_0 W$ is the total flow in the system, Q, and keeping in mind the definition of the Péclet number Eq. (40), we observe that Eq. (74) is again of the form $\mathrm{Pe} < \mathrm{Pe}_{\mathrm{thr}}(\Gamma)$. The functional form of $\mathrm{Pe}_{\mathrm{thr}}(\Gamma)$ in the rectangular case is different from that in the radial case, Eq. (69), but the stable region does exist in both geometries.

B. Relation to the Saffman-Taylor instability

The reactive-infiltration instability is an example of a broader class of processes in which a more mobile phase invades a less mobile one [26]. A paradigm problem of this kind is viscous fingering (Saffman-Taylor problem), where the less viscous fluid displaces the more viscous one in a Hele-Shaw cell. The dispersion relation for such a case reads [21]

$$\tilde{\omega} = \frac{\mu_d - \mu_u}{\mu_d + \mu_u}\tilde{k} - \mathrm{Ca}\frac{\tilde{k}^3}{12(1+\mu_d/\mu_u)}, \tag{75}$$

where k has been rescaled by the depth of the Hele-Shaw cell, b, and ω has been scaled by the corresponding timescale, $\tau = b/U_0$, where U_0 is the front velocity as before. Finally, $\mu_{u,d}$ are the viscosities of the invading and receding fluid and $\mathrm{Ca} = U_0\mu_u/\gamma$ is the capillary number, with γ—the interfacial tension.

The respective relation for the radial geometry reads [22]

$$\tilde{\omega} = \frac{\mu_d - \mu_u}{\mu_s + \mu_u}\tilde{n} - \mathrm{Ca}\frac{\left(\tilde{n}^3 - \tilde{n}\left(\frac{b}{R}\right)^2\right)}{12(1+\mu_d/\mu_u)} - \frac{b}{R}. \tag{76}$$

Comparison of these expressions with the respective dispersion relations for the reactive-infiltration instability leads to the following conclusions:

(1) As expected, the long-wavelength part of the Saffman-Taylor dispersion relation Eq. (75) is determined by the mobility contrast between the phases. Note that in viscous fingering the mobility contrast between the phases is related to the difference in viscosities between the invading (less viscous) phase and displaced (more viscous) phase, thus $\tilde{\omega}(\tilde{k}) \sim \frac{\mu_d-\mu_u}{\mu_d+\mu_u}\tilde{k}$. In reactive-infiltration instability [Eq. (71)] we get $\tilde{\omega}(\tilde{k}) \approx \frac{K_u-K_d}{K_d+K_u}\tilde{k}$, which corresponds to the permeability contrast between more porous dissolved phase and the less porous undissolved one, but the general mechanism remains the same: a more mobile phase is invading a less mobile one.

(2) The short-wave parts of the dispersion relations are different, reflecting different short-scale stabilization mechanisms: surface tension in the case of Saffman-Taylor problem versus diffusion for the reactive-infiltration

(3) In radial geometry, both in reactive-infiltration instability and in the Saffman-Taylor problem, extra terms appear in the dispersion relation [compare Eqs. (66) and (76)]: $-1/\mathrm{Pe}$ in the former case versus $-b/R$ and $\tilde{n}(\frac{b}{R})^2$ in the latter. These terms shift the dispersion curve downwards, allowing for a stable displacement. Note, however, that the radial extent of the front, $R(t)$ is a function of time, which means that both b/R and $\tilde{n}(\frac{b}{R})^2$ approach zero in the long-time limit. This means that, eventually, the front always becomes unstable at a certain critical radius, as observed by Paterson [22]. Contrastingly, in the reactive infiltration, the negative term $(-1/\mathrm{Pe})$ does not depend on time thus the displacement remains stable. This leads to the appearance of the absolute regions of stability in Fig. 4. This difference is again due to the different stabilizing mechanisms in both cases. In Saffman-Taylor instability, the stabilizing factor is the surface tension, the effects of which depend linearly on the curvature. As the front advances, its radius increases, and thus the surface tension effects become weaker, unable to keep the system from becoming unstable. On the other hand, in the reactive-infiltration instability, the stabilization is due to diffusion, the effects of which are independent of the radius of curvature of the front.

C. Comparison with numerical simulations

A relatively large number of numerical simulations of the dissolution process have been performed over the years [6,12,13,27–29], in various setups and geometries. For the present study, the most relevant are the studies in radial geometry [13,18,19,30]. Most of these studies, however, are performed for relatively large heterogeneities of the medium, which makes it harder to observe the initial wavelengths of the instability (for the discussion of the interplay of heterogeneities in the initial conditions and instability mechanism, see Ref. [31]). Additionally, the flow velocities used are usually rather large, which places the system well in the unstable region in Pe-Γ space and makes it hard to observe the stability-instability transition. In this respect, the most relevant simulations are those of Cohen [32], who performed 2D radial simulations of dissolution for relatively uniform initial medium in large range of flow rates (cf. Fig. 4.13 in Ref. [32]). The simulations there were performed at the flow rates $Q = 1.8 \times 10^{-4}$ cm^2/s–18 cm^2/s, corresponding to Pe in the range of 2.9–2.9 $\times 10^5$ (note that Ref. [32] uses a different definition of the Péclet from the one used here). The permeability ratio was very close to zero, $\Gamma = 3 \times 10^{-8}$. The simulations at the lowest flow rate (Pe = 2.9) show stable displacement whereas those at Pe = 8.7 are already unstable, which is in agreement with Eq. (69) which gives $\mathrm{Pe}_{\mathrm{thr}} = 2/(2-\sqrt{3}) \approx 7.46$ at $\Gamma = 0$. Importantly, in this range of flow rates, the parameter H (12) remains large (10^3–10^4), thus the thin-front limit, adopted in the present work, holds.

D. Relation to the star patterns on ice

Equations (27)–(30) describing the dissolution of the porous medium share a lot of features with a process of melting of snow slush by the flowing water. The field driving the phase change is then different (temperature and not the concentration) but the positive feedback mechanism is the same: a small bump on an advancing interface between melted and unmelted regions will focus the flow and thus lead to the increased melting in its vicinity. This instability leads to the formation of star-like patterns on frozen lakes and rivers (Fig. 5)—whenever a hole forms in the ice cover, relatively warm (at 4° C) water flows to the surface and melts the snow layer [33,34]. In the photographs in Fig. 5 the flow lines of the water are also beautifully marked on the ice, which clearly shows the focusing of the flow at the tips of the fingers. Tsai and Wettlaufer [34,35] proposed a mathematical model of the advancing melting front which is essentially equivalent to Eqs. (27)–(30) with the only difference that an infinite permeability of the upstream part has been assumed. The dispersion relation for this model can then be obtained directly by applying Eq. (66) with $\Gamma = 0$, i.e.,

$$\tilde{\omega}(\tilde{n}) \equiv \tau\omega = [1 - \sqrt{1+4\tilde{n}^2} + \tilde{n}] - \frac{1}{\mathrm{Pe}}, \tag{77}$$

where this time Pe is the thermal Péclet number,

$$\mathrm{Pe} = \frac{Q}{2\pi\alpha}, \tag{78}$$

where α is the thermal diffusivity and φ_1 was assumed to be 1. Note that this is different from the dispersion relation reported in Refs. [34,35] due to a rather subtle point, which seems to be overlooked in these works. Namely, the driving force for the instability is the temperature profile in the upstream phase, which is a solution of the convection-diffusion Eq. (53). The flow field in this equation given by Eq. (52) can only be obtained assuming nonzero permeability contrast and only then carrying the limit $\Gamma \to 0$. Instead, in Ref. [35] the infinite permeability of the upstream part of the flow is assumed from the beginning and the upstream velocity perturbations are then obtained by an ansatz, which does not lead to a correct form of the upstream flow.

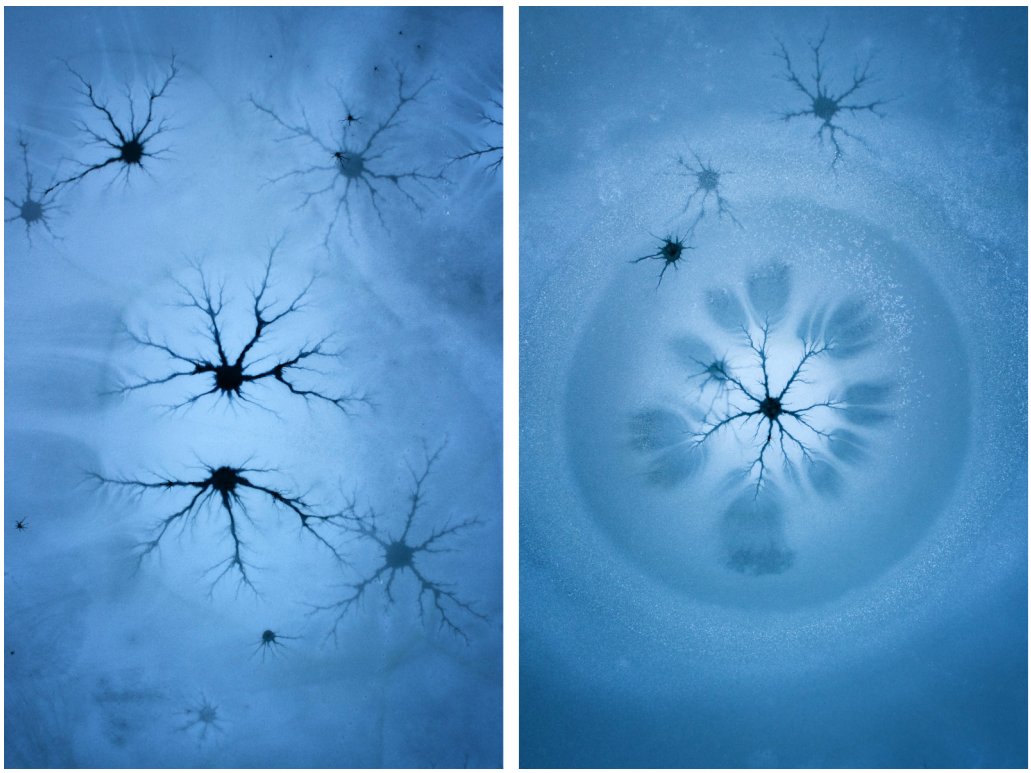

FIG. 5. Starlike patterns on a frozen lake. The photos are courtesy of Martin Mecnarowski (www.photomecan.eu).

To predict the instability wavelength, we need an estimate of the flow rate through the initial holes in the ice cover. A well-documented measurement of this value was not reported. The rough estimates [33] lead to the value of flow velocities around the circular hole of the order of 2×10^{-3} cm/s. The diameter of the holes if of the order of 10–40 cm [36]. This gives $Q \approx 2 - 8 \times 10^{-2}$ cm^2/s, which combined with $\alpha = 10^{-3}$cm^2/s [34] yields Pe $\approx$ 20–80. Finally, Eq. (67) with $\Gamma = 0$ gives $n_c \approx$ 5–20. This is compatible with the observations from Fig. 5—the patterns there have on average about 10 branches emanating from the main circle, some of them very short. The differences in lengths between the branches are natural in the context of unstable growth processes, as they reflect strong competition between neighboring fingers—the flow focuses in longer ones and recedes from the shorter ones. Additionally, the inner circle slowly expands, wiping out the traces of short, dead branches. These phenomena make it hard to estimate the original number of branches based on the fully grown, nonlinear pattern.

IX. SUMMARY

We have carried out the stability analysis of the front between the dissolved and undissolved medium in the radial geometry, when the reactive fluid is injected centrally into a porous block. We have adopted a thin front limit, in which the thickness of the front is small in comparison to the diffusive length. Linear stability analysis for the radial flow problem yields the dispersion relation $\omega(k)$, which shows that both long and short waves are unstable. The position of the maximum of $\omega(k)$ depends on both the Péclet number (Pe) and permeability contrast between the undissolved and dissolved phase (Γ). In particular, there is a range of (Γ, Pe) parameters in which the system is (linearly) stable, irrespectively of the radial extent of the front. This is in contrast to the Saffman-Taylor instability where the system is always unstable when the critical radius is reached. We also pointed out the similarities between the reactive-infiltration instability and the similar instability in the heat transfer, which is driving the formation of star-like patterns on frozen lakes.

ACKNOWLEDGMENTS

This work was supported by the National Science Centre (Poland) under research Grant No. 2012/07/E/ST3/01734. The authors benefited from discussions with Michał Bogdan, Le Xu, and Tony Ladd. Martin Mecnarowski is gratefully acknowledged for the photos of the ice star patterns.

[1] J. Chadam, D. Hoff, E. Merino, P. Ortoleva, and A. Sen, IMA J. Appl. Math. **36**, 207 (1986).
[2] P. Ortoleva, J. Chadam, E. Merino, and A. Sen, Am. J. Sc. **287**, 1008 (1987).
[3] G. Daccord, Phys. Rev. Lett. **58**, 479 (1987).
[4] G. Daccord and R. Lenormand, Nature **325**, 41 (1987).
[5] J. D. Sherwood, Chem. Eng. Sci. **42**, 1823 (1987).
[6] M. L. Hoefner and H. S. Fogler, AIChE J. **34**, 45 (1988).

[7] C. N. Fredd and H. S. Fogler, AIChE J. **44**, 1933 (1998).
[8] E. J. Hinch and B. S. Bhatt, J. Fluid Mech. **212**, 279 (1990).
[9] B. Jamtveit and Ø. Hammer, Geochem. Perspect. **1**, 341 (2012).
[10] P. J. Ortoleva, *Geochemical Self-Organization* (Oxford University Press, New York, 1994).
[11] B. Jamtveit and P. Meakin, *Growth, Dissolution and Pattern Formation in Geosystems* (Springer, Berlin, 1999).
[12] F. Golfier, C. Zarcone, B. Bazin, R. Lenormand, D. Lasseux, and M. Quintard, J. Fluid Mech. **457**, 213 (2002).
[13] C. E. Cohen, D. Ding, M. Quintard, and B. Bazin, Chem. Eng. Sci. **63**, 3088 (2008).
[14] P. Szymczak and A. J. C. Ladd, Earth Planet. Sci. Lett. **301**, 424 (2011).
[15] P. Szymczak and A. J. C. Ladd, Geophys. Res. Lett. **40**, 3036 (2013).
[16] G. Daccord, E. Touboul, and R. Lenormand, SPE Prod. Eng **4**, 63 (1989).
[17] G. Daccord, R. Lenormand, and O. Liétard, Chem. Eng. Sci. **48**, 169 (1993).
[18] N. Kalia and V. Balakotaiah, Chem. Eng. Sci. **62**, 919 (2007).
[19] P. Liu, G. D. Couples, J. Yao, Z. Huang, W. Song, and J. Ma, Comput. Geosci. **22**, 1187 (2018).
[20] L. Xu, P. Szymczak, R. Toussaint, E. G. Flekkøy, and K. J. Måløy, Front. Phys. **7**, 96 (2019).
[21] P. G. Saffman and G. Taylor, Proc. Roy. Soc. Lond. A **245**, 312 (1958).
[22] L. Paterson, J. Fluid. Mech. **113**, 513 (1981).
[23] P. Kondratiuk and P. Szymczak, SIAM J. Appl. Math. **75**, 2193 (2015).
[24] A. J. Ladd and P. Szymczak, Water Resour. Res. **53**, 2419 (2017).
[25] E. O. Dias and J. A. Miranda, Phys. Rev. E **88**, 013016 (2013).
[26] P. Pelcé, *New Visions on Form and Growth: Fingered Growth, Dendrites, and Flames* (Oxford University Press, Oxford, 2004).
[27] P. Szymczak and A. J. C. Ladd, Geophys. Res. Lett. **33**, L05401 (2006).
[28] M. Panga, M. Ziauddin, and V. Balakotaiah, AIChE J. **51**, 3231 (2005).
[29] R. L. Detwiler and H. Rajaram, Water Resour. Res. **43**, W04403 (2007).
[30] P. Liu, J. Yao, G. D. Couples, J. Ma, and O. Iliev, Sci. Rep. **7**, 17711 (2017).
[31] V. K. Upadhyay, P. Szymczak, and A. Ladd, J. Geophys. Res.: Solid Earth **120**, 6102 (2015).
[32] C.-E. Cohen, Modélisation et simulation de la stimulation acide des puits carbonatés, Ph.D. thesis, Institut National Polytechnique de Toulouse, 2007.
[33] C. A. Knight, in *Structure and Dynamics of Partially Solidified Systems*, edited by D. E. Loper (Martinus Nijhoff, The Hague, The Netherlands, 1987), pp. 453–465.
[34] V. C. Tsai and J. S. Wettlaufer, Phys. Rev. E **75**, 066105 (2007).
[35] V. C. Tsai, in *2006 Program of Studies: Ice (Geophysical Fluid Dynamics Program) (Woods Hole Oceanogr Inst Tech Report 2007-02)* (Woods Hole Oceanographic Institution, Woods Hole, 2007), pp. 272–285.
[36] K. B. Katsaros, Bull. Amer. Meteorol. Soc. **62**, 1446 (1981).